

Hydronium Intercalation Enables High Rate in Hexagonal Molybdate Single Crystals

Haocheng Guo, Sicheng Wu, Wen Chen, Zhen Su, Qing Wang, Neeraj Sharma, Chengli Rong, Simon Fleischmann, Zhaoping Liu,* and Chuan Zhao*

Rapid proton transport in solid-hosts promotes a new chemistry in achieving high-rate Faradaic electrodes. Exploring the possibility of hydronium intercalation is essential for advancing proton-based charge storage. Nevertheless, this is yet to be revealed. Herein, a new host is reported of hexagonal molybdates, $(A_2O)_x \cdot MoO_3 \cdot (H_2O)_y$ ($A = Na^+, NH_4^+$), and hydronium (de)intercalation is demonstrated with experiments. Hexagonal molybdates show a battery-type initial reduction followed by intercalation pseudocapacitance. Fast rate of 200 C ($40 A g^{-1}$) and long lifespan of 30 000 cycles are achieved in electrodes of monocrystals even over 200 μm . Solid-state nuclear magnetic resonance confirms hydronium intercalations, and operando measurements using electrochemical quartz crystal microbalance and synchrotron X-ray diffraction disclose distinct intercalation behaviours in different electrolyte concentrations. Remarkably, characterizations of the cycled electrodes show nearly identical structures and suggest equilibrium products are minimally influenced by the extent of proton solvation. These results offer new insights into proton electrochemistry and will advance correlated high-power batteries and beyond.

competing with each other such that improvements in one feature will often comprise the other. Solid-state ion diffusion is limiting the kinetics in faradaic electrodes, and the phenomenon of intercalation pseudocapacitance (rapid solid-solution ion insertion)^[2] provides a possible solution from material perspectives to balance the rate and capacity.^[3] Kinetics of ion diffusion also depend strongly on the choice of ion-charge-carrier. Proton is the lightest and smallest among all ions and is fast in transport. Furthermore, protons can be rapidly transported through a unique Grotthuss mechanism, which is a structural diffusion of H^+ through a chain of water molecules via concerted cleavage/formation of hydrogen/covalent bonds.^[4] Proton-based interactions are known to promote (pseudo)capacitive behaviors at the surfaces of some electrodes such as porous carbon and $RuO_2 \cdot nH_2O$,^[5] but rarely studied in battery fields. Recently, the new

chemistry of proton batteries is emerging with discoveries of correlated electrodes,^[6] and excellent performances are achieved benefitting from the fast transport of proton-ions, such as high rate behaviors at 4000 C from a defective Prussian blue analogue.^[7]

Comprehending the underlying mechanisms is crucial for advancing new battery chemistries. In the realm of proton electrochemistry, a pivotal question arises given that protons predominantly exist as hydronium ions ($H^+(H_2O)_n$) in aqueous


1. Introduction

Electrochemical energy storage is indispensable for the efficient harvest and distribution of electricity from fluctuant and intermittent renewables. Developing faradaic electrodes that simultaneously possess high capacity of batteries and fast rate and long lifetime of supercapacitors is highly attractive.^[1] However, this has been challenging because rate and capacity are normally

H. Guo, S. Wu, Z. Su, N. Sharma, C. Rong, C. Zhao
School of Chemistry
University of New South Wales
Sydney, NSW 2052, Australia
E-mail: chuan.zhao@unsw.edu.au

H. Guo, W. Chen, Z. Liu
Advanced Li-ion battery lab
Ningbo Institute of Material Technology and Engineering
Chinese Academy of Science
Ningbo 315200, P. R. China
E-mail: liuzp@nimte.ac.cn

Q. Wang
School of Chemical Sciences
The University of Auckland
Auckland 1142, New Zealand
S. Fleischmann
Helmholtz Institute Ulm
89081 Ulm, Germany

 The ORCID identification number(s) for the author(s) of this article can be found under <https://doi.org/10.1002/adma.202307118>

© 2023 The Authors. Advanced Materials published by Wiley-VCH GmbH. This is an open access article under the terms of the Creative Commons Attribution-NonCommercial-NoDerivs License, which permits use and distribution in any medium, provided the original work is properly cited, the use is non-commercial and no modifications or adaptations are made.

DOI: 10.1002/adma.202307118

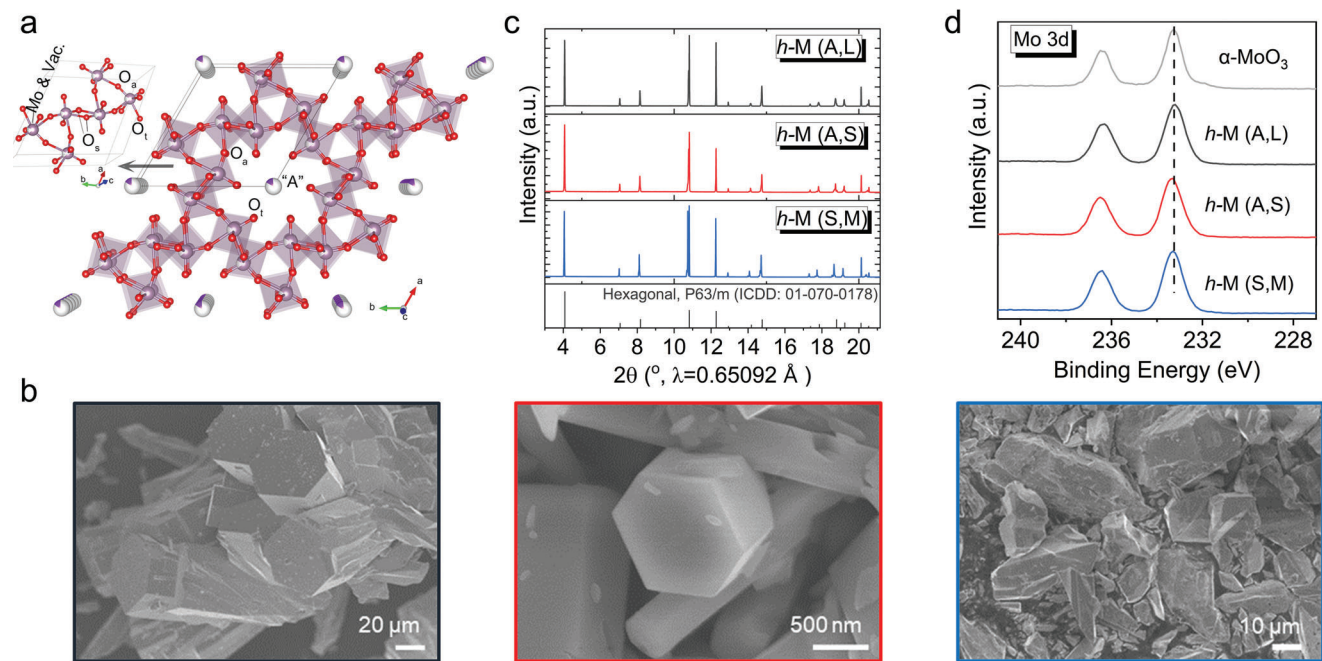


Figure 1. Physical properties of hexagonal molybdates. a) Crystal structure of a representative hexagonal molybdate ($K_{0.31}Mo_{4.85}O_{15}OH(H_2O)_2$, ICDD: 01-070-0178). b) From left to right, SEM images of crystallites of *h*-M (A, L), *h*-M (A, S), and *h*-M (S, M), respectively. c) Synchrotron XRD patterns of the three samples and d) XPS Mo 3d spectra of hexagonal molybdates and α - MoO_3 .

solutions: is naked proton or hydronium(s) intercalating into electrode hosts? This question is of paramount significance in unraveling fundamental proton-ion intercalation processes. The intercalation of hydronium has been proposed in a study of organic pigment via simulation (2017)^[8] and the hypothesis was then adopted by several reports concerning oxides.^[9,10] However, through experiments and (or) simulations, a number of studies disclose naked proton (de)intercalation and transport to occur instead, despite there is sufficient room/volume for hosting hydronium and (or) water within electrode materials. Rapid Grotthuss proton conduction is reported in open framework materials of Prussian blue analogues^[7] and 2D atom sheets of $Ti_3C_2T_x$ MXenes^[11] where percolating crystal water channels are present. Alternatively, a non-Grotthuss proton diffusion mechanism through lattice oxygens is revealed in the hydrous oxide of $WO_3 \cdot 2H_2O$,^[12] and a similar naked proton transport is verified in anhydrous oxides of α - MoO_3 ,^[13,14] and anatase TiO_2 .^[15] Furthermore, hydronium desolvation^[14,15] has been identified, which influence the electrode cycling stability significantly.^[14,16] Following that, strategies like tuning proton solvation in aqueous electrolytes,^[17,18] developing anhydrous electrolytes^[19,20] and facilitating hydronium desolvation via artificial interfaces^[21] are found effective in stabilizing electrode cycling. Nevertheless, high energy barriers are reported for hydronium desolvation,^[22] and the important question remains whether hydronium intercalation is possible, and if yes how would it behave?

Herein, we show the structural chemistry of a new host of hexagonal molybdates and report experimental evidence of hydronium (de)intercalation. Hexagonal molybdates can generally be formulated as $(A_2O)_x \cdot MoO_3 \cdot (H_2O)_y$ (A = alkali metal or ammonium, etc.),^[23] and they present unique tunnel-structures (Figure 1a) which are necessarily defective with additional chan-

nel cations compensating the Mo vacancies in frameworks.^[24] These materials are also known as “hexagonal MoO_3 ” in literatures and this has raised continuing confusions:^[24] because “hexagonal MoO_3 ” refers to an ideally stoichiometric (channel cation absent) structure which however is never achieved. The materials have excellent electrical conductivity^[25] and are therefore highly promising for high-power applications. In this study, a series of hexagonal molybdates (denoted as *h*-M) with different particle sizes and channel cations (Na^+ , NH_4^+) are prepared and the electrochemical-structural reactions are systematically investigated in electrolytes of sulfuric acids. We determine hydronium intercalation into *h*-M via solid-state nuclear magnetic resonance (ssNMR), and analyze the ion-electrode-interactions through real-time monitoring of electrode mass and structure evolutions by electrochemical quartz crystal microbalances (EQCM) and operando synchrotron X-ray diffraction (SXRD). Remarkably, we find evidence of dynamic hydronium intercalation behaviors and demonstrate fast rate and long cycle life of *h*-M monocrystal electrodes with particles sizing even over 200 μm . Comprehensive characterizations are also performed on cycled electrodes to gain further insight to the structural transitions and understand the relationship between structure and electrochemical properties.

2. Results and Discussions

2.1. Structure and Characterization of Hexagonal Molybdates

The structure of hexagonal molybdates is illustrated in Figure 1a, according to the first reported potassium phase.^[26] *h*-M is made up of double chains of edge-sharing and strongly distorted $[MoO_6]$ octahedra. The chains are linked via vertices and produce

hexagonal-rings and triangles on the *ab* plane. These chain connections are intrinsically defective because of statistical Mo deficiencies in the unit cell. Along the *c* axis tunnels are present where structure cations (“A”) are located to compensate charge, generating a 3D prism structure. *h*-M structure is related to α -MoO₃^[14] with similar three types of lattice oxygens: (i) “terminal oxygen” (O_t) with unsaturated Mo–O_t bond pointing to the center of the hexagonal-ring, (ii) “asymmetric oxygen” (O_a) results in another unsaturated Mo–O_a bond with two Mo ions in one direction, and (iii) “symmetric oxygen” (O_s) presenting three-fold symmetry as they share vertices of three adjacent [MoO₆] octahedra. Overall, *h*-M possess large intracrystalline space accompanied with unsaturated lattice oxygens, which therefore are available to host a variety of foreign species, and a series of mono-valence cations (e.g., Na⁺, NH₄⁺, Ag⁺,^[27] K⁺, Cs⁺, etc.) and molecules (e.g., crystal water) are reported in synthetic *h*-M materials. Hence, the *h*-M could theoretically allow electrochemical intercalation of water molecules and a variety of cations. It should be noted, however, whether ions and (or) molecular species can insert into the crystal lattice is not simply a matter of “size”, which will be discussed later.

From scanning electron microscope (SEM) results (Figure 1b; Figure S1, Supporting Information), representative hexagonal rods can be observed in all *h*-M samples with channel ammonium (i.e., A = NH₄⁺), and we choose two samples of large and small crystallites for the following study, which are labelled as *h*-M (A, L) or AL, and *h*-M (A, S) or AS, respectively. *h*-M (A, L) samples have the largest crystallites with the cross-section dimension over 50 μ m (Figure 1b, left) and length even exceeding 200 μ m (Figure S1a, Supporting Information). *h*-M (A, S) is comprised of small crystallites, and the rod diameter is about 1 μ m (Figure 1b, middle) with an average length of \approx 3 μ m. *h*-M with channel sodium (i.e., A = Na⁺) are also prepared where 30–50 μ m particles can be found with morphologies of rectangular blocks and pyramidal rods (Figure 1b right and Figure S1c, Supporting Information). This sample serves as an appropriate middle contrast and is designated as *h*-M (S, M)/SM. Different appearances are noticed in the powders of these three materials (Figure S1d, Supporting Information). Synchrotron powder X-ray diffraction (XRD) data were collected (Figure 1c). All three samples present strong reflections and can be well indexed to the displayed reference pattern (K_{0.31}Mo_{4.85}O₁₅OH(H₂O)₂, ICDD: 01-070-0178) which crystallizes with hexagonal symmetry and P6₃/m space group. *h*-M (S, M) displays more obvious (210)/(101) peak splitting (around 10.8°) possibly because of the Na⁺ occupying a special position and the corresponding additional water molecules within the channels.^[24]

Figure 1d displays X-ray photoelectron spectroscopy (XPS) results, and it is found all three *h*-M materials present identical profiles as the reference sample (α -MoO₃) where their Mo 3d_{5/2} bands lie between 232 and 233 eV indicating the exclusive oxidation state of Mo (VI).^[28] Fourier transform infrared (FTIR) spectra confirm the presence of crystal water in all three materials and detect N-H bonds from ammonium-containing materials (Figure S2, Supporting Information). Thermogravimetry analysis in combination with mass spectra has then been adopted to determine the content of volatile species (Figures S3–S5 and Note S1, Supporting Information). The mass loss from 100 to 430 °C is attributed to evapora-

tion of H₂O and NH₃ from the sample lattice, and the three materials show mass drops of 4.36% (AL), 3.77% (AS), and 3.08% (SM). In combination with (semi-)quantitative elemental analysis of XPS, the chemical compositions of the three materials are estimated to be [(NH₄)₂O]_{0.145}MoO₃(H₂O)_{0.24} for AL, [(NH₄)₂O]_{0.15}MoO₃(H₂O)_{0.18} for AS, and (Na₂O)_{0.07}MoO₃(H₂O)_{0.26} for SM (Tables S1 and S2 and Note S2, Supporting Information). These compositions can also be expressed in the Mo atom deficient form as, (NH₄)_{0.277}Mo_{0.95}O₃(H₂O)_{0.23} (AL), (NH₄)_{0.29}Mo_{0.95}O₃(H₂O)_{0.17} (AS), and Na_{0.14}Mo_{0.98}O₃(H₂O)_{0.26} (SM).

2.2. Electrochemical Properties of Hexagonal Molybdates

Because electrochemical performance often correlates to the size of electrode material, we focused the investigation on the medium-sized sample, i.e., *h*-M (S, M), then analyzed the possible influence(s) of crystallite sizes. Figure 2a shows the cyclic voltammetry (CV) of *h*-M (S, M). Two main reduction processes are observed in the first reductive scan, i.e., a minor broad peak (R1) around 0.05 V (vs SCE, unless otherwise noted) then a prominent peak (R2) centered at approximately –0.2 V, which indicates a battery-type ion intercalation. In the reverse scan, a broad peak symmetric to R1 (O1, \approx 0.1 V) is present while a small hump (O2) is observed around –0.15 V, suggesting an irreversible initial process. In the 2nd cycle, there is only one reduction peak (R', \approx –0.16 V) identified with reduced applied current, and the oxidation process displays a broad overall hump. These signatures of redox peaks decrease gradually in the following cycles and overall CV profiles transform to a more rectangular-like shape below 0 V (e.g., cycle 05 and other scans in Figure S6 in the Supporting Information), which is reminiscent of (pseudo-)capacitive charge storage process.^[29] Galvanostatic charge–discharge (GCD) profiles in Figure 2b are consistent with the CV results. Correlating to R1 and R2 peaks in CV, a short slope and a long plateau are observed in the first reduction, delivering an initial capacity of around 368 mAh g^{–1} (equivalent to \approx 2.1 electrons transferred per Mo, calculated according to the estimated composition). The subsequent charge-discharge curves (e.g., cycle 02, 03) display a linear responses of electrode potential (*U*) with respect to capacity (*Q*) at regions below 0 V, which is characteristic of (pseudo)capacitive charge storage. Similar performances are also found in a diluted electrolyte concentration (1.0 M H₂SO₄, Figure S7, Supporting Information). All these characteristics suggest a reversible pseudocapacitive charge storage for hexagonal molybdates following the initial battery-like process.^[29] Furthermore, when examined through CV measurements with varying scan rates (Figure S8, Supporting Information), dominant capacitive contributions are confirmed where the value exceeds 90% at 20 mV s^{–1}.

Figure 2c highlights the initial reduction profiles of the three *h*-M samples. Similar capacities are delivered for the medium and large-sized *h*-M samples and in both electrolyte concentrations, despite overpotential differences. In *h*-M (A, S) containing the smallest particles, higher capacity (\approx 400 mAh g^{–1}) is obtained which can be partly attributed to increased side reactions of electrolytes, and we observed similar capacity increase in another proton electrode when reducing particle sizes.^[14,30] Additionally, it is

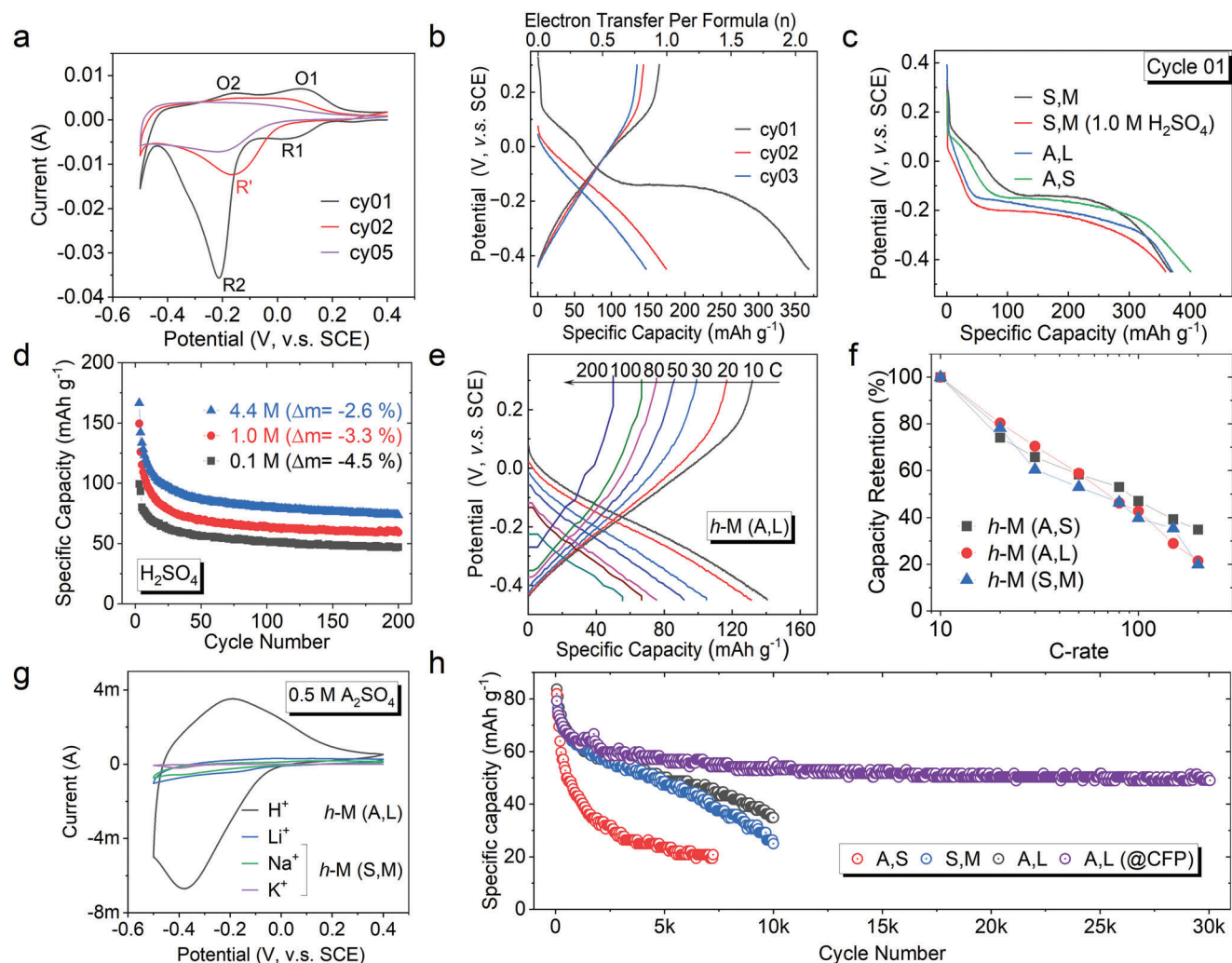


Figure 2. Electrochemical characteristics of hexagonal molybdates. a) CV profiles and b) GCD curves of initial cycles of *h*-M (S, M), at a scan rate of 3 mV s^{-1} and constant current of 5 C ($1 \text{ C} = 200 \text{ mA g}^{-1}$), respectively. c) The first galvanostatic reduction step of different *h*-M electrodes under 5 C currents. d) The cycling performances of thick *h*-M (S, M) electrodes in different electrolyte concentrations. e) GCD curves of *h*-M (A, L) electrodes at different C-rates, and corresponding f) capacity retention profiles of the three electrodes under increasing C-rates. g) CV profiles of *h*-M (A, L) in $0.5 \text{ M H}_2\text{SO}_4$ and *h*-M (A, S) in $0.5 \text{ M Li}_2\text{SO}_4/\text{Na}_2\text{SO}_4/\text{K}_2\text{SO}_4$ at a scan rate of 5 mV s^{-1} . h) Long-term cycling stability of the three samples. Active materials loaded on titanium mesh and $4.4 \text{ M H}_2\text{SO}_4$ were adopted as the electrodes and electrolytes unless otherwise noted.

found that *h*-M (S, M) presents the least electrode polarization, indicating the channel cation (NH_4^+ vs Na^+) is more important than particle size in influencing the conductivity. Figure 2d shows the cycling performances of thick *h*-M (S, M) electrodes in different electrolyte concentrations. Similar trends are observed that decrease on initial cycles and stabilize gradually in the following cycles. The initial decreases in capacity are accompanied with increases of coulombic efficiency (CE, as shown in Figure S9 in the Supporting Information), suggesting that the electrochemical reversibility of all three groups improves in the initial cycles, and the $4.4 \text{ M H}_2\text{SO}_4$ group exhibits the highest CE which stabilizes at 100%. The observed initial performance decay can be attributed to electrode dissolution^[14,19,31] as electrode weight-loss is identified in post-cycled electrodes, which present close values of 97.4% (4.4 M), 96.7% (1.0 M), and 95.5% (0.1 M) of their original mass. Importantly, the following cycles maintain generally stable capac-

ity regardless of electrolyte concentrations, and this is notably different from other proton electrodes which degrade rapidly in diluted electrolytes.^[14,16] Furthermore, significantly higher capacities are achieved in aqueous electrolytes compared to anhydrous electrolytes (Figure S10, Supporting Information). These observations imply a different ion intercalation mechanism in hexagonal molybdates.

Figure 2e displays GCD profiles of *h*-M (A, L) with increasing applied current, which demonstrates an excellent rate capability in electrodes even with hundred-micrometer-sized particles. Figure 2f and Figure S11 (Supporting Information) display rate performances of the other samples. *h*-M (A, S) shows the best performances thanks to small particle sizes, while all three samples show generally consistent capacity retention with increasing C-rates. The similar maximum capacity and rate capability of *h*-M suggest electrochemical activities with proton/hydronium

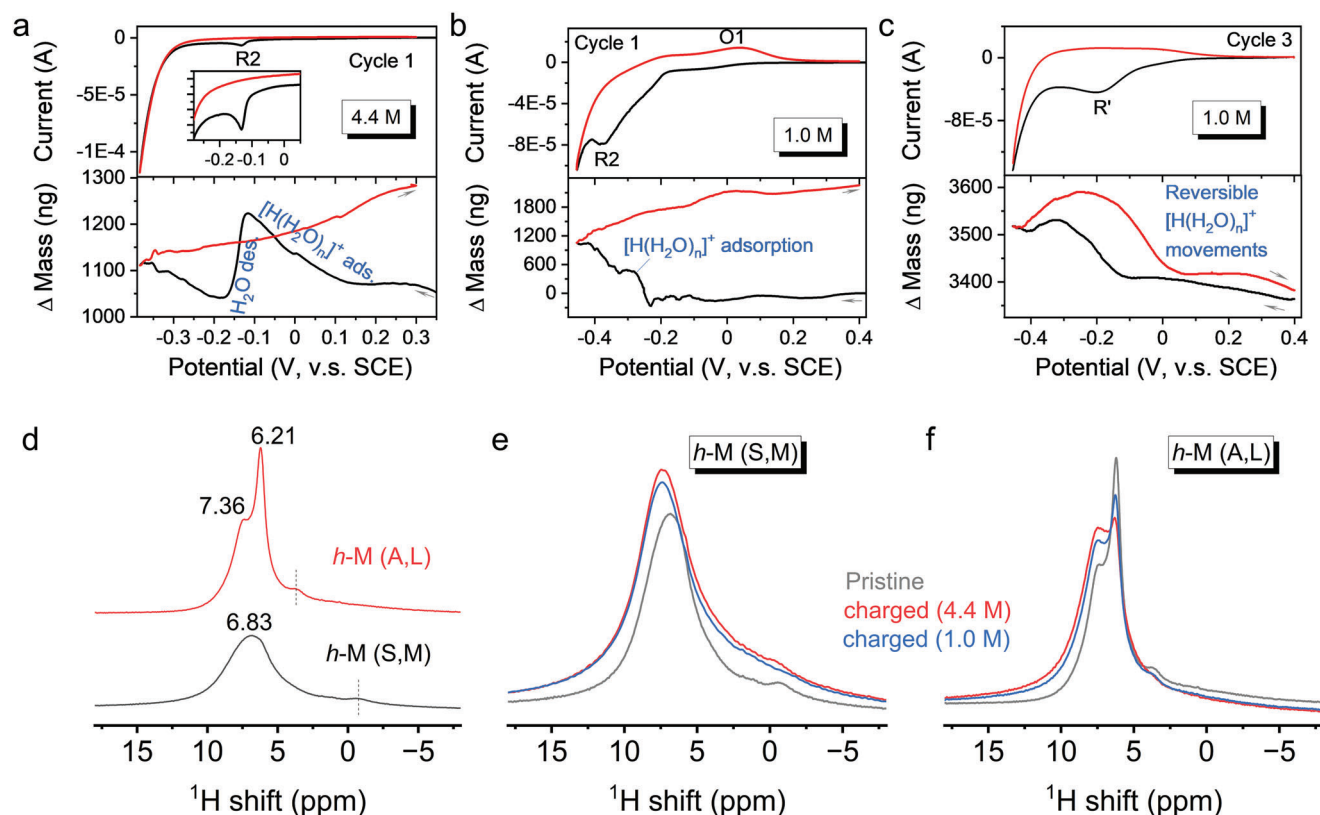


Figure 3. Interfacial reaction and hydronium intercalation. EQCM results of *h*-M (S, M) in a) 4.4 M H_2SO_4 , and b,c) 1.0 M H_2SO_4 . 1H ssNMR spectra of d) pristine electrodes of *h*-M (A, L) and *h*-M (S, M), and charged electrodes (cycle 1) in different electrolyte concentrations of e) *h*-M (S, M) and f) *h*-M (A, L), respectively. NMR signals were normalized based on sample masses.

are irrelevant to particle size and morphologies. In comparison, the particle size of *h*-M is crucial for redox activities with metal cations. As shown in Figure 2g and Figures S12 and S13 (Supporting Information), prominent CV profiles of *h*-M (A, L) electrodes are observed in 0.5 M H_2SO_4 since the beginning, but little redox activity of the electrodes is noticed in 0.5 M Li_2SO_4 . When using *h*-M (A, S) electrodes of the smallest crystallites, certain active electrochemical signals can be found in A_2SO_4 ($A = Li, Na, K$) electrolytes but repeated cycles are required for activation. The size of metal-ion also shows an impact on performance, with higher electrochemical activities obtained for Li^+ than Na^+ and K^+ . Interestingly, superior redox activities of *h*-M are obtained with NH_4^+ than K^+ , despite having similar ionic sizes, which is possibly facilitated by the potential hydrogen bonding to the lattice oxygen.^[32] These data suggest the ion intercalation into *h*-M is not solely a matter of size, for both particle and electrolyte-ion. While the particle size of *h*-M shows little influence on capacity and rate, we found a significant impact on cycling stability. Figure 2h displays the cycling stability of different *h*-M electrodes in 4.4 M H_2SO_4 . A clear dependence on electrode particle size can be identified where large crystallite size facilitates high cycling stability, and the *h*-M (A, L) electrodes sustain the most stable cycling over 30 000 cycles. Overall, the hexagonal molybdate single crystals show superior electrochemical performances (Table S3, Supporting Information).

2.3. Detection of Hydronium Intercalation

h-M shows unique cycling performance non-sensitive to water contents in electrolytes. This indicates a different ion-intercalation mechanism compared to previous findings on naked proton (de)intercalation.^[7,14,15] EQCM experiments were conducted to monitor real-time electrode mass change and study interfacial reactions. Figure 3a,b displays the first cycle CV and corresponding mass–potential (m – E) curves of *h*-M (S, M) electrodes in 4.4 and 1.0 M H_2SO_4 , respectively. The CV profiles show noticeable signals of electrolyte reduction (hydrogen evolution) because of the low active mass loading on gold surfaces, while the characteristic redox processes at -0.13 V are clearly presented. Regarding the mass change, naked protons are negligible in weight therefore electrode mass evolutions can be mainly attributed to the solvent water of proton solvation shell. In 4.4 M H_2SO_4 , a gradual mass increase is observed in the cathodic scan from 0.2 V till the peak potential of the R2 process and followed by a sharp mass drop. The mass increase agrees with the direction of cationic flux and corresponds to hydronium adsorptions on electrodes. The following mass change shows an inverse process which suggests hydronium desolvation and water desorption.^[14] By contrast, a monotonic mass increase trend through the R2 range is observed in 1.0 M H_2SO_4 suggesting net hydronium adsorption. This difference can be attributed to the higher level of

water solvation of hydroniums in 1.0 M H₂SO₄ than 4.4 M H₂SO₄, and high energy barrier for hydronium desolvation.^[15,22]

In the subsequent cycles, a mass increase is observed for both electrolytes suggesting overall accumulation of hydroniums and solvent water on electrodes.^[10,14,17] In particular, a subtle mass evolution in the oxidation process of the 1.0 M H₂SO₄ is noted (Figure 3b), where the electrode mass increases slightly then decreases across the O1 region. This can be attributed to the solvation of deintercalated ions (e.g., low-extent-solvated hydronium) at electrode surfaces followed by ion desorption.^[14] Similar mass behavior is identified in the second cycle in 1.0 M H₂SO₄ (Figure S14, Supporting Information), while reversible hydronium adsorption/desorption is observed in the following cycles with little change of electrode mass (Figure 3c; Figure S14, Supporting Information). Overall, EQCM measurements disclose distinct surface interactions of hydroniums with *h*-M electrodes, which are because of different ion-solvation-extents of bulk electrolytes and have an impact on the subsequent ion intercalation steps to be disclosed later.

¹H ssNMR characterization is further carried out to probe hydrogen signals of a series of electrodes and investigate whether the adsorbed hydroniums are inserted in the lattices. Figure 3d shows the spectra of the pristine samples, where different proton-containing species are found. In *h*-M (A, L), two main proton environments are identified, one presents as a sharp peak at ≈6.21 ppm, and the other as a splitting shoulder at about 7.36 ppm. The narrow 6.21 ppm signal is attributed to strongly hydrogen-bonded ammonium species of the lattice, and the broad peak at 7.36 ppm is ascribed to water molecules confined within the crystal.^[33] The assignments are supported by their spinning sideband (ssb, Figure S15, Supporting Information), that the less significant 7.36 ppm signal yields a more intense ssb instead because of the strong dipolar coupling of H₂O.^[14] Additionally, a weak threshold signal around 3.61 ppm (indicated by the dashed line in Figure 3d) is observed in *h*-M (A, L) which is possibly induced by an isolated hydroxyl group.^[34] Similar features are observed in the ammonium-free sample of *h*-M (S, M), and only one broad chemical shift peak around 6.83 ppm is related to the crystal water. A weak signal at approximately −0.67 ppm is detected and is also attributed to the presence of a solitary −OH group, similar to *h*-M (A, L). This assignment primarily relies on their comparable signal amplitudes, and similar trends of signal reduction are discernible in their charged electrodes (where hydrogen is predominantly removed). On the other hand, the differences in their chemical shifts might imply variations in chemical environments for the H nucleus in the two composites, which could possibly be influenced by their composition and/or specific atomic arrangements.^[24]

Evolutions of crystal water are highlighted by spectra of *h*-M (S, M) in Figure 3e. The main signals and ssb (Figure S15, Supporting Information) of both cycled electrodes become more intense in comparison to the pristine. These indicate increased contents of crystal water and confirm the water/hydronium intercalation. Slight peak broadenings are also noticed and suggest a relatively disordered environment. The signals are found shifted to higher ppm which can be attributed to strengthened hydrogen bonds in accumulated water molecules. It has been reported monomeric water molecules yield a proton resonance at around 2 ppm while cluster states produce a typical signal at 4.8 ppm.^[35] Furthermore,

the 1.0 M H₂SO₄ sample shows close but slightly lower intensity than that of the 4.4 M H₂SO₄ sample. This might imply a comparatively severer material dissolution due to the intercalation of high solvation extent hydronium. Similar crystal water evolutions are also observed in *h*-M (A, L) samples as shown in Figure 3f. Additionally, weaker signals of N–H species are identified in cycled electrodes, which can be a result of (electro-)chemical extraction of NH₄⁺. Interestingly, channel Na⁺ is removed completely after a whole discharge–charge cycle based on XPS results (Figure S16, Supporting Information), while obvious resonance of N–H species is still present, thus indicating the coexistence of certain crystal ammonia molecules in (cycled) *h*-M. These in return imply a similar possibility of interchange between hydronium and water inside the lattice.

2.4. Structural Chemistry of Hydronium Insertion into Hexagonal Molybdates

Operando synchrotron XRD experiments were performed to illustrate the dynamic hydronium (de)intercalation reactions. As shown in Figure 4a,b, constant reflections of the hexagonal molybdate (designated as H phase) are first observed in both electrolytes until the end of R1, which suggest a possible surface reaction of hydronium adsorptions. Following that, the major reduction process of R2 initiates and since there notable distinctions are observed between the two electrolytes.

In 4.4 M H₂SO₄ (Figure 4a), new reflection signals become noticeable at stage (iii), which are positioned at lower 2θ values compared to the (100) and (210)/(101) peaks of the H phase. These signals correspond to an unidentified intermediate (labelled with *arrow* and denoted as the U1 phase), indicating a two-phase reaction. Progressing with the R2 reduction (stage (iii) to (v)), the U1 phase increases in intensity and shows a slight change in peak position, suggesting a solid solution reaction of U1 (that continues till the U1 phase disappears). Meanwhile, peak intensities of the original H phase decrease notably. Across the R2 peak (stage (vi)), these reflections of U1 lose intensity and two new reflections appear (indicated by *star*) that are associated with another unidentified phase designated as U2. This is the second two-phase reaction and results in three phases being present. To the R2 end (stage (vii) to (viii)), intensities of the U2 phase are the most prominent, while signals from the U1 and H phases diminish and ultimately vanish at stage (vii) and (viii) respectively. Upon further reaction ((ix) to (xii)), there remains only the U2 phase present which undergoes solid-solution reactions as evidenced by the continuously changing peak positions and the peak intensity stays generally consistent. To facilitate a better understanding of the structure changes, a semi-quantitative analysis has been performed on the discussed phases, as shown in Figure 4c and Figure S17 in the Supporting Information. This analysis is based on fitted peak area of the initial peaks, given that the identification of the detected new phases remains highly challenging due to the limited number of reflections. Overall, the structure evolution can be summarized as (1) two sets of two-phase reactions, (2) a minute solid-solution reaction between the two two-phase reactions, and (3) a subsequent solid-solution reaction on discharge.

By contrast, in 1.0 M H₂SO₄ (Figure 4b), all peaks of the original H phase persist throughout the whole CV process. At the

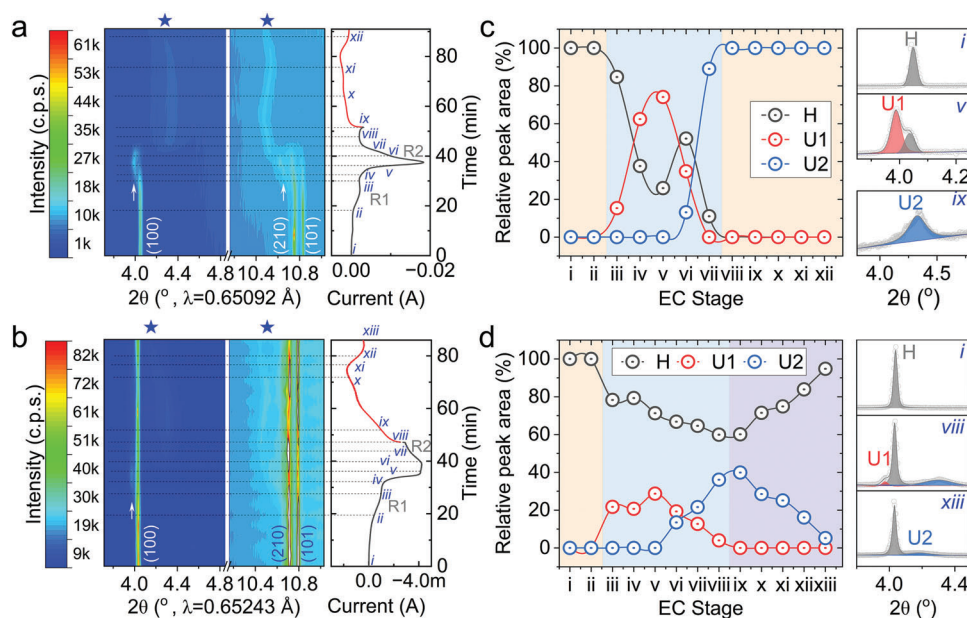


Figure 4. Structural evolution of *h*-M (S, M). Operando synchrotron XRD contour plots of hexagonal molybdates (denoted as H) in a) 4.4 m and b) 1.0 m H_2SO_4 electrolytes. Arrow indicates an intermediate unidentified structure (U1), and star suggests another unknown phase (U2). Relative peak areas of initial reflections in the three phases for the c) 4.4 m and d) 1.0 m H_2SO_4 electrolyte groups. Colors in (c) and (d) highlight the monophasic (orange) and multiphasic (blue) regions, and the fitted profiles at selected stages from three regions are displayed adjacent highlighting the phase evolution.

same time, the same extra reflections (as in 4.4 m H_2SO_4) are also observed, suggesting the discussed reactions take place at similar stages but to a “lower” extent. Interestingly, in the oxidation process, it is found the U2 phase also decreases in intensity in addition to position shifts. This is also substantiated in the quantitative analysis (Figure 4d; Figure S18, Supporting Information) and only trace U2 phase is present when oxidation ends.

The behavior of two-phase and solid-solution reactions with ion insertion is commonly observed for layered materials, such as de-lithiation of LiCoO_2 to $\text{Li}_{0.5}\text{CoO}_2$ where the two phases are typically Li-rich and Li-poor structures of similar compositions or slightly distorted lattices,^[36] and diffusion-limited (battery-type) charge storage is accompanied. In our results, intercalation steps result in the formation of additional phases (peak disappearance/appearances) and changes in phase volume (peak shifts), which indicates a battery-type initial reduction. This reduction is however irreversible, as the transformed structure does not revert in the subsequent stages. The possible reason lies in the hydronium intercalation process, which involves the incorporation of highly polarized water molecules, potential deformations of the hydronium configuration, and the formation of strong covalent bonds ($-\text{OH}$) between the exposed proton core and lattice oxygen. These various factors collectively influence the internal electrical field of the material, leading to adjustments in atomic positions and an increase in strains and Gibbs energy. Consequently, despite the large intracrystalline space, irreversible phase transitions are initiated to achieve a more stable structure for reversible hydronium (de)intercalation. The observed distinctions in structure evolutions of the two electrolyte groups can accordingly be ascribed to the intercalation of hydroniums with varying degrees of solvation, which well aligns with the EQCM results. Combined with electrochemical results, it is evident that hydro-

num (de)intercalation becomes reversible following the initial reduction and facilitates charge storage of intercalation pseudo-capacitance in the subsequent cycles for both electrolytes.

Diffraction results of specific state-of-charge (SOC) electrodes are then analyzed. In Figure 5a, distinctly different from the operando results, the *ex situ* patterns (4.4 M H_2SO_4 group) surprisingly reveal reflections of both the U2 and H phases at discharge/charge states. Additionally, trace amounts of the U1 phase are detected in the discharged electrode. This phenomenon can be possibly attributed to several reasons: (1) the new phase (U2) is a kinetically accessed structure, and relaxation leads to the formation of *h*-M, and/or (2) the operando experiments record a metastable or transient phase possibly not at equilibrium,^[37] and (3) these three structures are very similar in energy and can be interchanged (reversibly) to certain extents. In 1.0 m H_2SO_4 , the real-time data (Figure 4b,d) already illustrate the diffraction signals of *h*-M as well as the new structure(s), and *ex situ* tests yield consistent results, with multiple phases present and identical patterns revealed in both electrolyte groups (Figures S19 and S20, Supporting Information) This indicates the equilibrium products comprise of both *h*-M and the additional phase(s). Similar *ex situ* XRD results are also confirmed in different *h*-M samples and both electrolytes (Figures S19 and S20, Supporting Information). Overall, it is demonstrated the intercalation of hydronium ions with different degrees of solvation has a negligible impact on the final equilibrium products. After extended cycling, all reflections are retained with no additional signal detected (Figure S21, Supporting Information), confirming the reversibility of the reactions. Nevertheless, a reduction in crystallinity can be observed.

X-ray absorption spectra (XAS) at Mo K-edge was performed to probe the overall Mo valence change and local structure variation. Figure 5b shows the X-ray absorption near edge spectra

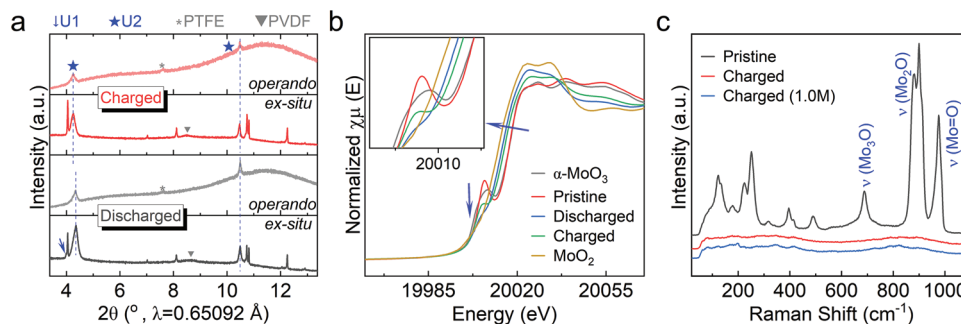


Figure 5. Post-reaction structure analysis of *h*-M (S, M). a) Comparisons of extracted real-time X-ray diffraction patterns with *ex situ* results of cycled electrodes in 4.4 M H₂SO₄. b) K-edge XANES of the electrode series and references of molybdenum oxides. c) Raman spectra of pristine and charged electrodes.

(XANES). The K-edges of *h*-M are verified at the highest energy as that of α -Mo^{VI}O₃, while the value is lower for the discharged electrode but higher than that of Mo^{IV}O₂. A small positive edge shift follows when charging the electrode back. This confirms the evolution of Mo valance states for charge compensation which agrees with the XPS analysis (Figure S16, Supporting Information). Furthermore, pre-edges are also identified. The pre-edge structure is ascribed to quadruple electron excitation and is diagnostic of the symmetry of metal ions,^[38] for instance α -MoO₃ presents a strong pre-edge peak thanks to the distorted [Mo^{VI}O₆] octahedra and signals are lost in MoO₂ because the excitation is forbidden in perfect octahedra symmetry of [Mo^{IV}O₆] (Figure S22, Supporting Information). Regarding the electrode series, the pristine *h*-M shows an even stronger pre-edge peak than α -MoO₃ reference suggesting more distorted [MoO₆] octahedra. Significantly reduced intensities are observed in both SOC electrodes indicating the reduction of Mo ion with more octahedral symmetries. Pre-edge signals almost disappear in the discharged electrode and accord with the white line energy, suggesting the lowest Mo valance state with the most ion insertion. Slightly different local environments for the discharged/charged electrodes are observed in the extended X-ray absorption fine-structure spectra (EXAFS, Figure S23 and Table S4, Supporting Information). Note, the XAS results of SOC electrodes herein were tested after relaxation, therefore deviations from the operando conditions are possible due to the subtle structure changes.

Raman spectra were finally conducted to investigate surface evolutions. As shown in Figure 5c and Figure S24 (Supporting Information), a series of scattering signals are observed in the pristine electrode that correspond to the Raman features of hexagonal molybdates.^[39] Specifically, the three main peaks at high wavenumbers are characteristic of vibrations of Mo₃O (\approx 688 cm⁻¹), Mo–O–Mo (882, 898 cm⁻¹), and Mo=O (975 cm⁻¹) bonds, respectively.^[40] In contrast, charged samples in both electrolytes display only minor vibrations which spread over two broad hump regions. SEM images (Figure S25, Supporting Information) show the presence of intragranular cracks on particles of charged electrodes, and electrochemical impedance spectroscopy (EIS, Figure S26, Supporting Information) measurements reveal an increase in charge transfer resistance. These results collectively suggest surface degradation after the initial process and agree with the overall decrease of crystallinity observed. Completing an extended cycling process, the interfacial

resistance remains generally unchanged (Figure S26, Supporting Information). Considering the observed reduction in crystallinity (Figure S21, Supporting Information) and electrode mass loss (Figure 2d) during cycling, it can be inferred the primary cause of performance decay is the electrochemical dissolution of active materials.

3. Conclusion

In summary, hydronium (de)intercalation is demonstrated in a new host of hexagonal molybdates. Testing in sulfuric acids, *h*-M evolves from a battery-type initial discharge to intercalation pseudocapacitance, and consistent findings apply in samples with different sizes and structural cations (Na⁺, NH₄⁺). Particle size is found to be less influential on rate performances but promotes the cycling stability. A high-rate capability of 200 C (40 A g⁻¹) and a long cycling life of 30 000 cycles are achieved in electrodes of single crystals sizing even over 200 μ m. In comparison, electrochemical activities of *h*-M in A₂SO₄ electrolytes (A = Li, Na, K) show strong size dependences on both particle and ion-charge-carrier. Hydronium intercalation into *h*-M is confirmed by ssNMR from intensified crystal water signals. Different ion-electrode-interactions in two electrolyte concentrations are disclosed in real-time via EQCM and operando SXRD, and electrodes in 1.0 M H₂SO₄ show no obvious desolvation and maintains largely the pristine structure. Interestingly, the subsequent analysis of cycled electrodes reveal nearly identical structures in both electrolytes, suggesting the varying degrees of proton solvation have minimal impact on the equilibrium products. Benefiting from hydronium intercalation, electrode cycling stability is insensitive to electrolyte concentrations. However, material electrochemical dissolution still occurs and accounts largely for the cycling degradation. These findings will have significant implications for developing future proton electrodes and hopefully advance progresses of corresponding high-power batteries and beyond.

Supporting Information

Supporting Information is available from the Wiley Online Library or from the author.

Acknowledgements

C.Z. is thankful for the financial support from the Australian Research Council (FT170100224, IC200100023, CE230100017). The authors acknowledge the UNSW Digital Grid Futures Institute for the award of 2021 Interdisciplinary Seed Fund. Z.L. is grateful for the fund from Natural Science Foundation of China (51872305). H.G. acknowledges the financial support of UNSW Science PhD writing scholarship. The authors thank Australian Synchrotron for the awards of PD and XAS beam-time. The authors are grateful for Dr. Xinmiao Liang and Dr. Aditya Rawal for helps in NMR tests and interpretations. The authors thank Dr. Anita D'Angelo for assistance in the synchrotron PD experiments, Dr. Yuhuan Zhou for fruitful discussions, Prof. Cai Shen and Mrs. Xin Zhang for providing EQCM apparatus.

Open access publishing facilitated by University of New South Wales, as part of the Wiley - University of New South Wales agreement via the Council of Australian University Librarians.

Conflict of Interest

The authors declare no conflict of interest.

Data Availability Statement

The data that support the findings of this study are available from the corresponding author upon reasonable request.

Keywords

hexagonal molybdates, hydronium intercalation, operando XRD, single-crystal electrode, solid-state NMR

Received: July 18, 2023
Revised: November 1, 2023
Published online:

- [1] P. Simon, Y. Gogotsi, B. Dunn, *Science* **2014**, *343*, 1210.
- [2] V. Augustyn, J. Come, M. A. Lowe, J. W. Kim, P.-L. Taberna, S. H. Tolbert, H. D. Abruña, P. Simon, B. Dunn, *Nat. Mater.* **2013**, *12*, 518.
- [3] S. Fleischmann, J. B. Mitchell, R. Wang, C. Zhan, D. E. Jiang, V. Presser, V. Augustyn, *Chem. Rev.* **2020**, *120*, 6738.
- [4] C. De Grotthuss, *Ann. Chim. Phys.* **1806**, *58*, 54.
- [5] J. P. Zheng, P. J. Cygan, T. R. Jow, *J. Electrochem. Soc.* **1995**, *142*, 2699.
- [6] H. Guo, C. Zhao, *Small Methods* **2023**, e2300699.
- [7] X. Wu, J. J. Hong, W. Shin, L. Ma, T. Liu, X. Bi, Y. Yuan, Y. Qi, T. W. Surta, W. Huang, J. Neufeind, T. Wu, P. A. Greaney, J. Lu, X. Ji, *Nat. Energy* **2019**, *4*, 123.
- [8] W. Xingfeng, B. Clement, J. Zelang, L. Zhifei, R. S. Chandrabose, I. A. Rodriguez-Perez, G. P. Alex, J. Xiulei, *Angew. Chem., Int. Ed.* **2017**, *56*, 2909.
- [9] H. Zhang, W. Wu, Q. Liu, F. Yang, X. Shi, X. Liu, M. Yu, X. Lu, *Angew. Chem., Int. Ed.* **2021**, *60*, 896.
- [10] H. Jiang, J. J. Hong, X. Wu, T. W. Surta, Y. Qi, S. Dong, Z. Li, D. P. Leonard, J. J. Holoubek, J. C. Wong, J. J. Razink, X. Zhang, X. Ji, *J. Am. Chem. Soc.* **2018**, *140*, 11556.

- [11] Y. Sun, C. Zhan, P. R. C. Kent, M. Naguib, Y. Gogotsi, D.e-E.n Jiang, *ACS Appl. Mater. Interface* **2019**, *12*, 763.
- [12] H. Lin, F. Zhou, C.-P. Liu, V. Ozolins, *J. Mater. Chem. A* **2014**, *2*, 12280.
- [13] Z. Ma, X.-M. Shi, S.-I. Nishimura, S. Ko, M. Okubo, A. Yamada, *Adv. Mater.* **2022**, *34*, 2203335.
- [14] H. Guo, D. Goonetilleke, N. Sharma, W. Ren, Z. Su, A. Rawal, C. Zhao, *Cell Rep. Phys. Sci.* **2020**, *1*, 100225.
- [15] C. Geng, T. Sun, Z. Wang, J.-M. Wu, Y.-J. Gu, H. Kobayashi, P. Yang, J. Hai, W. Wen, *Nano Lett.* **2021**, *21*, 7021.
- [16] X. Peng, H. Guo, W. Ren, Z. Su, C. Zhao, *Chem. Commun.* **2020**, *56*, 11803.
- [17] Z. Su, J. Chen, W. Ren, H. Guo, C. Jia, S. Yin, J. Ho, C. Zhao, *Small* **2021**, *17*, e2102375.
- [18] S. Wu, J. Chen, Z. Su, H. Guo, T. Zhao, C. Jia, J. Stansby, J. Tang, A. Rawal, Y. Fang, J. Ho, C. Zhao, *Small* **2022**, *18*, e2202992.
- [19] Y. Xu, X. Wu, H. Jiang, L. Tang, K. Y. Koga, C. Fang, J. Lu, X. Ji, *Angew. Chem., Int. Ed.* **2020**, *59*, 22007.
- [20] M. Liao, X. Ji, Y. Cao, J. Xu, X. Qiu, Y. Xie, F. Wang, C. Wang, Y. Xia, *Nat. Commun.* **2022**, *13*, 6064.
- [21] C. Wang, S. Zhao, X. Song, N. Wang, H. Peng, J. Su, S. Zeng, X. Xu, J. Yang, *Adv. Energy Mater.* **2022**, *12*, 2200157.
- [22] W. A. Donald, R. D. Leib, M. Demireva, J. T. O'Brien, J. S. Prell, E. R. Williams, *J. Am. Chem. Soc.* **2009**, *131*, 13328.
- [23] N. A. Caiger, S. Crouch-Baker, P. G. Dickens, G. S. James, *J. Solid State Chem.* **1987**, *67*, 369.
- [24] E. M. Mccarron, D. M. Thomas, J. C. Calabrese, *Inorg. Chem.* **1987**, *26*, 370.
- [25] A. Chithambararaj, N. Rajeswari Yogamalar, A. C. Bose, *Cryst. Growth Des.* **2016**, *16*, 1984.
- [26] B. Krebs, I. Paulat-Böschen, *Acta Crystallogr., Sect. B: Struct. Crystallogr. Cryst. Chem.* **1976**, *32*, 1697.
- [27] J. Guo, P. Zavalij, M. S. Whittingham, *J. Solid State Chem.* **1995**, *117*, 323.
- [28] a) J. Chastain, R. C. King Jr, *Perkin-Elmer Corporation* **1992**, *40*, 221 b) T. H. Fleisch, G. J. Mains, *J. Chem. Phys.* **1982**, *76*, 780.
- [29] Y. Gogotsi, R. M. Penner, *ACS Nano* **2018**, *12*, 2081.
- [30] Z. Su, W. Ren, H. Guo, X. Peng, X. Chen, C. Zhao, *Adv. Funct. Mater.* **2020**, *30*, 2005477.
- [31] M. Liao, Y. Cao, Z. Li, J. Xu, Y. Qi, Y. Xie, Y. Peng, Y. Wang, F. Wang, Y. Xia, *Angew. Chem., Int. Ed.* **2022**, *61*, e202206635.
- [32] S. Dong, W. Shin, H. Jiang, X. Wu, Z. Li, J. Holoubek, W. F. Stickle, B. Key, C. Liu, J. Lu, P. A. Greaney, X. Zhang, X. Ji, *Chem* **2019**, *5*, 1537.
- [33] H.-J. Lunk, H. Hartl, M. A. Hartl, M. J. G. Fait, I. G. Shenderovich, M. Feist, T. A. Frisk, L. L. Daemen, D. Mauder, R. Eckelt, A. A. Gurinov, *Inorg. Chem.* **2010**, *49*, 9400.
- [34] D. Mauder, D. Akcakayiran, S. B. Lesnichin, G. H. Findenegg, I. G. Shenderovich, *J. Phys. Chem. C* **2009**, *113*, 19185.
- [35] N. Masaru, W. Chihiro, *Chem. Lett.* **1992**, *21*, 809.
- [36] N. Sharma, V. K. Peterson, M. M. Elcombe, M. Avdeev, A. J. Studer, N. Blagojevic, R. Yusoff, N. Kamarulzaman, *J. Power Sources* **2010**, *195*, 8258.
- [37] D. Li, H. Zhou, *Mater. Today* **2014**, *17*, 451.
- [38] Y.-N. Zhou, J. Ma, E. Hu, X. Yu, L. Gu, K.-W. Nam, L. Chen, Z. Wang, X.-Q. Yang, *Nat. Commun.* **2014**, *5*, 5381.
- [39] V. V. Atuchin, T. A. Gavrilova, V. G. Kostrovsky, L. D. Pokrovsky, I. B. Troitskaia, *Inorg. Mater.* **2008**, *44*, 622.
- [40] L. Seguin, M. Figlarz, R. Cavagnat, J.-C. Lassègues, *Spectrochim. Acta, Part A* **1995**, *51*, 1323.